Geophys. J. R. astr. Soc. (1976) **46**, 575–593

Motions Near a Shallow Rupturing Fault: Evaluation of Effects Due to the Free Surface

J. G. Anderson*

Lamont-Doherty Geological Observatory of Columbia University, Palisades, New York 10964, USA and Department of Geological Sciences, Columbia University, USA

(Received 1976 March 11; in original form 1975 November 3)

Summary

The displacement of the surface of a half space near a shallow rupturing fault is, generally, approximated poorly by doubling the amplitude calculated for the same source in an infinite space. To obtain this result, the motions of a half space were calculated using a Green's function which is a solution to Lamb's problem, and the motions of an infinite space were calculated using the formulae of Haskell. A good approximation to the half-space displacement caused by a *P*- or *S*-wave incident at most angles from a point source is numerical correction of the displacement resulting from the point source in an infinite space for the amplification and phase shift of a plane-wave incident at a free surface. This correction approximately doubles the amplitude of the infinite space displacement for *SV*-waves with angles of incidence within 30 degrees of vertical, for *P*-waves within 70 degrees of vertical, and for all *SH*-waves. The static offset of the free surface from a point source is not, in general, twice the offset calculated in the corresponding infinite space case. The displacement from an extended fault is calculated by superposition of point sources on the fault plane; when the infinite space amplitudes may be doubled for all (or most) of these point sources, it may also be doubled for the extended source.

Introduction

The surface motions resulting from a point source in a half space include four major effects which are absent in an infinite space: The amplification of all waves; the phase shift of *SV*-waves incident at angles greater than critical; the *SP*-phase, which travels to the surface as an *SV*-wave at the critical angle and is then refracted horizontally as a *P*-wave; and Rayleigh waves. These effects have all been studied before from a point source (e.g. Knopoff *et al.* 1957; Pekeris & Lifson 1957; Kawasaki, Suzuki & Sato 1973); the present objective is to evaluate the effect of including the free surface when the source is a spatially-extended rupture. This allows a critical evaluation of the assumption, used frequently in dislocation modelling, that the free surface may be reasonably accounted for by doubling the amplitude of motions in an

*Present address: Division of Engineering and Applied Science, California Institute of Technology, Pasadena, California 91125, USA.

infinite space (e.g. Kanamori 1972; Trifunac 1974; Trifunac & Udwadia 1974; Anderson 1974).

Method

The displacements of the surface of a half space are calculated by applying the representation theorem (Burridge & Knopoff 1964):

$$U_i(\mathbf{x}, t) = \int_{-\infty}^{\infty} dt' \iint_S \mu n_k(\boldsymbol{\xi})[u_j(\boldsymbol{\xi}, t')]\big(g_{ij,k'}(\mathbf{x}, t-t'; \boldsymbol{\xi}, 0) + g_{ik,j'}(\mathbf{x}, t-t'; \boldsymbol{\xi}, 0)\big)\, d\xi_1\, d\xi_3. \quad (1)$$

Here U_i is the ith component of displacement of the surface, μ the shear modulus, n_k the kth component of the normal to the fault, and $[u_j]$ the amplitude of the dislocation on the fault. The integration is over time and the fault surface. The Green's function is

$$g_{ij,k'} = \frac{d}{d\xi_k} g_{ij},$$

where g_{ij} is the displacement in the i direction at location $\mathbf{x}$, time t due to an impulse force in the j direction at location $\boldsymbol{\xi}$, time t'. Thus, $g_{ij,k'}$ is the displacement due to a

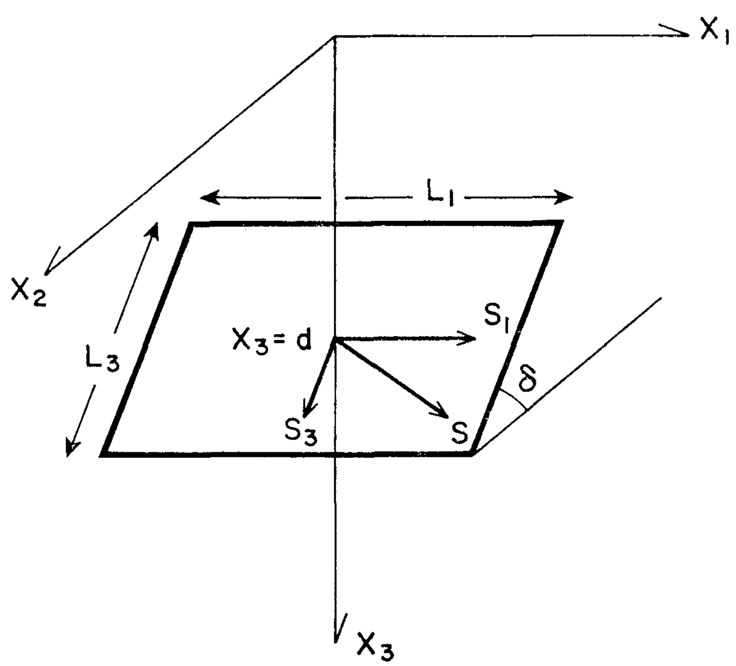

FIG. 1. Co-ordinate system and faulting parameters. The plane $x_3 = 0$ is the free surface. The fault strikes in the x_1 direction, and the dip δ is measured from the horizontal plane. The point $(x_1, x_2, x_3) = (0, 0, d)$ is the geometrical centre of the fault, and the origin of the (ξ_1, ξ_3) co-ordinates (not shown) which describe a point on the fault plane. The direction of slip on the fault is given by the unit vector s, with components S_1 (in the ξ_1 direction) and S_3 (in the ξ_3 direction) giving respectively the relative amplitudes of strike-slip and dip-slip motion.

point couple, and the sum $(g_{ij,k'}+g_{ik,j'})$ is the displacement due to a double-couple force, or, equivalently, due to a point dislocation. It is of the form

$$g_{ij,k'} = \frac{d^2}{dt^2} h_{ij,k'}$$

where $h_{ij,k'}$ is evaluated by an integral in the complex plane given by Johnson (1974). The differentiation must be done numerically. As a function of time $t_0 = t-t'$, $h_{ij,k'}$ is a Green's function for a force which is zero for $t_0 < 0$ and has magnitude t_0 for $t_0 > 0$.

This series of integrations and differentiations was handled as follows:

Step 1. The Green's functions are computed (using a Romberg integration subroutine) and stored for an array of points on the fault. The differentiation with respect to time is deferred until the second step. These are computed only once for each fault-station geometry.

Step 2. The source time function for each grid point is convolved with the corresponding Green's function to perform the time integral. The results from all the points on the fault plane are weighted and summed to perform the spatial integration. The weight of a grid point is the area of the fault inside a rectangle, centred on the grid point, with sides equal to the grid spacing. Thus, the sum of the weights is equal to the fault area. The sum of the convolved functions is differentiated numerically to obtain the desired displacement at the station.

Because the spatial limits of integration are a function of time, it is necessary to justify taking the time differentiation outside the spatial integral. This is allowable because the integration is approximated numerically by a sum, where the weight of the Green's function for each grid point is independent of time. The errors due to this approximation are discussed below. Because the weights are constants, it does not matter whether the sum or the numerical differentiation is done first.

In finding a dislocation model for an earthquake, the fault-station geometry is known, and displacements at the station are typically calculated for several trial models of rupture. The two-step method is excellent in this situation, because storing the Green's functions as in step 1 is more economical than recomputing them.

The displacements from a dislocation in an infinite space are calculated as described in Anderson & Richards (1975). The co-ordinate system for all models is shown in Fig. 1. The P-wave velocity $\alpha = 6{\cdot}0\ \mathrm{km\,s^{-1}}$ and the S-wave velocity $\beta = 3{\cdot}4\ \mathrm{km\,s^{-1}}$ was used throughout.

A propagating ramp dislocation time function is used here, but any other time function could have been used. In this model,

$$[u(\xi_1, \xi_3, t)] = \begin{cases} 0 & |\xi_1| > \dfrac{L_1}{2} \text{ or } |\xi_3| > \dfrac{L_3}{2} \\ 0 & t - t_r \leqslant 0 \\ \dfrac{D_m}{\tau}\left(t - t_r\right) & 0 < t - t_r < \tau \\ D_m & \tau \leqslant t - t_r \end{cases}$$

where L_1, L_3 are the fault dimensions, v is the rupture velocity, τ is the rise time, D_m is the final displacement on the fault, and t_r is $(\xi_1 + L_1/2)/v$.

Four integrals must be approximated by sums to compute displacement at a station on a half space. These approximations are sources of errors in the final waveform because only a finite number of sums can be done on a computer. Approximating the three integrations shown explicitly in equation (1) gives rise to an upper limit (f_s, say) to the frequencies which are meaningfully represented in the computed displacements. A method of evaluating f_s is presented next. Then the effect of errors from approximating the integration to obtain the Green's function is considered.

To estimate f_s, consider a source with an impulse time function travelling with velocity v along a short line of length L. The radiation at a distant station is a square wave, with duration T_0 and amplitude 1, say. The Fourier amplitude spectrum is

$$F_e(\omega) = T_0 \frac{\sin X}{X}$$

where $X = \omega T_0/2$. A model for this source by summing the radiation from two stationary points at the ends gives an approximate waveform

$$f_a(t) = \frac{T_0}{2}\,\delta\left(t+\frac{T_0}{2}\right) + \frac{T_0}{2}\,\delta\left(t-\frac{T_0}{2}\right).$$

The Fourier amplitude spectrum for this approximation is

$$F_a(\omega) = T_0 \cos X.$$

At zero frequency both the approximate and the exact spectra have amplitude T_0 and zero slope, but as $|X|$ increases they diverge. We introduce X_s as the upper limit on values of $|X|$ for which F_a is a satisfactory approximation to F_e. X_s should almost certainly be given a value less than 1, for at $X = 1$, F_a is only about two-thirds of F_e. For a propagating fault, Ben-Menahem (1961) showed

$$X = \frac{\omega L}{2c}\left(\frac{c}{v} - \cos\theta\right)$$

where c is the wave propagation speed and θ is the angle between the direction of

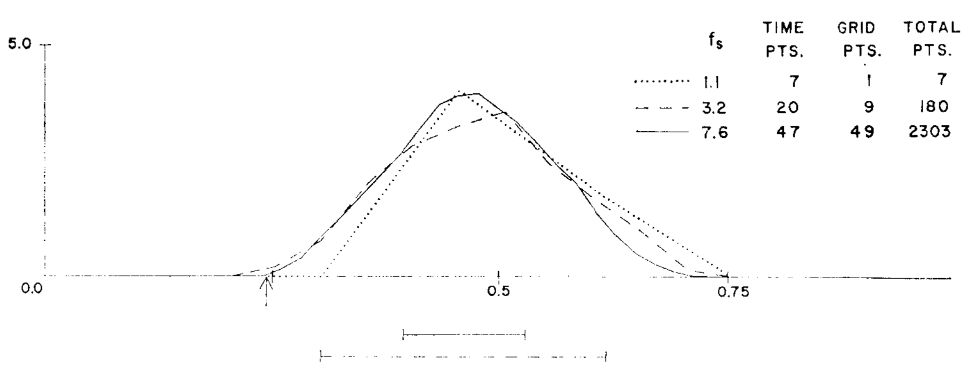

FIG. 2. A model evaluated using three values of f_s, with the Green's function in step 1 replaced by the non-physical function $h = (1/R)\,H(t-R/\alpha)$ (see text). The table gives the values of f_s (in Hz), and the corresponding number of time points, grid points, and total points at which the function h was evaluated. For each calculation, the line beneath the time axis has a length $T_s = f_s^{-1}$. For this calculation $(x_1, x_2) = (0{\cdot}866\text{ km}, 0{\cdot}5\text{ km})$, $d = 0{\cdot}5$ km, $\delta = 90°$. The rupture model is a propagating ramp with $L_1 = 1{\cdot}0$ km, $L_3 = 1{\cdot}0$ km, $v = 3{\cdot}0\text{ km s}^{-1}$, $\tau = 0{\cdot}2$ s.

rupture propagation and the direction to the receiver. If $|X| < X_s$, then the frequencies f which are adequately represented are given by

$$f = \frac{\omega}{2\pi} < \frac{c}{\pi L} \frac{X_s}{\left(\frac{c}{v} - \cos\theta\right)} = f_s.$$

Thus, a more dense grid spacing is needed to obtain displacements at backward angles from the direction of rupture propagation. For the cases of this paper, we use the simplified estimate $f_s = \beta/\pi L$, which can be derived using X_s less than 0·8 for our source receiver geometries. For other cases, particularly where $\theta > \pi/2$ or for small rupture velocities, the exact formula should be used.

Computer time is in general proportional to f_s^3. Two powers of f_s arise because the distance L is used as the spacing of Green's functions on the fault in both co-ordinate directions. The third power arises because for a larger f_s the Green's function must be calculated at a greater number of points in time. Here, waves at frequency f_s are sampled at a rate of six times per cycle.

The effect of f_s may be illustrated by replacing the Green's function in step 1 with the nonphysical function

$$h = \frac{1}{R} H(t - R/\alpha),$$

where H is the Heaviside step function and R is the distance between the grid point on the fault and the receiver. The discontinuity in h is typical of realistic Green's functions. A model is shown in Fig. 2, using this function h, for three values of f_s. These values required, respectively, 7, 180 and 2303 total evaluations of h in space and time. Thus, each successively greater value of f_s caused over an order of magnitude increase in computer time. The lines beneath the time axis in Fig. 2 show the time interval $T_s = f_s^{-1}$ for each value of f_s. One obvious inaccuracy is that the computed waves do not begin at the theoretical arrival time shown by the arrow. This discrepancy is inevitable for the case with only one grid point, as that point is not at the origin of rupture. For the other two cases, where a grid point is at the origin of rupture, the discrepancy originates in the numerical second derivative. In all cases, the difference between the time when the computed wave becomes non-zero and the theoretical arrival time is considerably shorter than T_s. The waveform would not be much different for values of f_s larger than the largest shown, where the duration of the wave is about four times T_s.

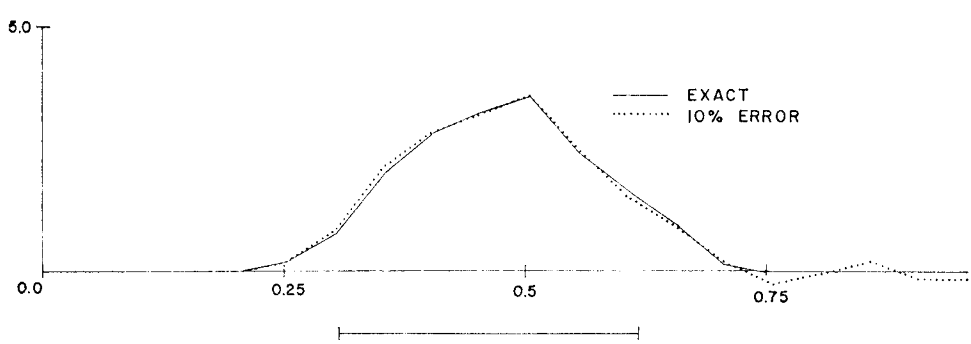

FIG. 3. The effect of introducing a 10 per cent random error to each of the 180 evaluations of h (in space and time) in the second case of Fig. 2.

The integration to evaluate the Green's function in step 1 is the final major source of errors in the computed waveform. This is done in a Romberg integration subroutine (Wilf 1967), which forms a series of estimates to the integral, doubling the number of points in the integrand for each successive estimate. It uses this series to predict the value of the integral, and returns an answer when two successive predictions differ by less than a specified relative error (ε, say). In computing the Green's function for a series of times in step 1, the answer for each time could have a random error, or the answers may be systematically too large or too small. Fig. 3 shows the effect a large random error may have on the second waveform in Fig. 2. To obtain the waveform with errors in Fig. 3, each point in time of each of the nine Green's functions was multiplied by a random value between 0·9 and 1·1. The result is quite similar to the answer without errors, indicating that random errors in step 1 have little effect upon the solution.

Numerical evaluation of the integral given by Johnson (1974) to obtain the Green's function often gives a result which is systematically slightly too large or too small. To be sure this systematic effect is negligible, it is necessary to repeat calculations changing only the relative error parameter ε until the resultant waveform no longer changes when ε is decreased further toward zero. Such trials indicated that $\varepsilon = 10^{-3}$ is adequate to reliably calculate displacements, but throughout this paper we use $\varepsilon = 10^{-4}$ or smaller.

The half space Green's functions were subjected to several tests, to be sure they are computed correctly. These will now be mentioned briefly before proceeding to some comparisons of half space and infinite space displacements.

1. Displacements agreed with Figs 7, 8 and 9 of Johnson (1974).

2. First motions were in the proper directions.

3. Rayleigh waves have retrograde elliptical particle motion.

4. Symmetry properties: All components of radiation from several sources showed the expected behaviour of being either even or odd, depending on the source, in both x and y.

5. The static offsets were in accord with results of Sato & Matsuura (1974).

6. Wave equation: Using reciprocity, a Green's function $g_{ij,k'}$ will obey the wave equation for a receiver fixed on the free surface when the source location is varied to compute the spatial derivative. As programmed, the terms $g_{ij,k'}+g_{ik,j'}$ in equation (1) are summed algebraically. For P-waves, $g_{ij,k'} = g_{ik,j'}$, and computed displacements were shown to obey the wave equation. The S-component lacks this symmetry, and could not be subjected to this test.

The comparison in the next section of half-space and infinite-space displacements from a point dislocation source may also be regarded as a mutual check of the half-space and infinite-space calculations.

Numerical examples: point dislocation sources

Dynamic displacements at a distance r from a point dislocation source in an infinite space consist of five components: two far-field terms which decrease as r^{-1}, two intermediate field terms which decrease as r^{-2}, and the near-field term which decreases as r^{-4} (Haskell 1969).

A comparison of motions from a point dislocation in a half-space and in an infinite space serves two purposes. First, it shows how well the far-field components from a point source in an infinite space (which can be quickly computed) can be

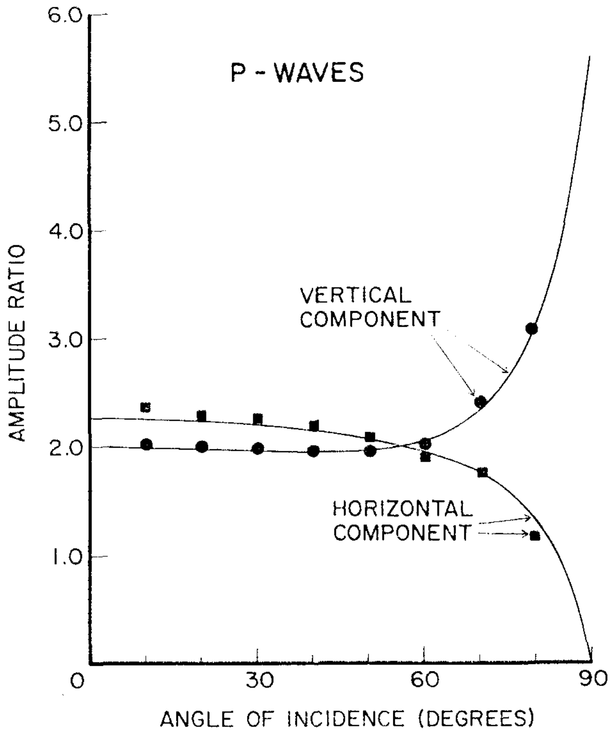

FIG. 4. Theoretical ratios (solid lines) of the amplitude of vertical and horizontal components of *P*-waves on a free surface to the amplitudes of the same component of the incoming wave (see Appendix equations (A1) and (A2)). The angle of incidence is measured from the normal to the surface. The data points are these ratios derived from computations with a point source Green's function.

corrected using plane wave theory to obtain the corresponding components in the half space. Second, it shows how the near and intermediate field displacements are affected by the free surface.

Displacements were calculated at eight stations, chosen such that in the half-space direct rays have angles of incidence (measured from the normal to the surface) which varied from 10 to 80 degrees in 10-degree intervals. We used two sources, both on a vertical fault: one was strike slip and the other was dip slip. The stations are on the x_2 axis, so that far field radiation is entirely *SH* from the strike-slip source, and entirely *P–SV* from the dip-slip source. Note that the displacements for the *SH* case cannot be calculated by the source-image method because the dislocation source causes *P*- and *SV*-far-field motions elsewhere in the $x_3 = 0$ plane.

From these calculations, the free surface amplification was derived for a far-field body wave by dividing the computed amplitude for the half space by the corresponding amplitude for the infinite space case. For *P*-waves, the computed ratios are shown in Fig. 4, and for *SV*-waves, these ratios are shown in Fig. 5.

The half space *SH* waves had the same wave shape as the whole space waves, and twice the amplitude, to within 3 per cent. This agrees well with theory, which predicts that exactly twice the amplitude should be expected at all angles of incidence.

For *P*- and *SV*-waves, the theoretical amplification of waves by the free surface is given by equations in the Appendix. Corresponding theoretical curves are plotted in Fig. 4 for *P*-waves and Fig. 5 for *SV*-waves, together with the ratios of the com-

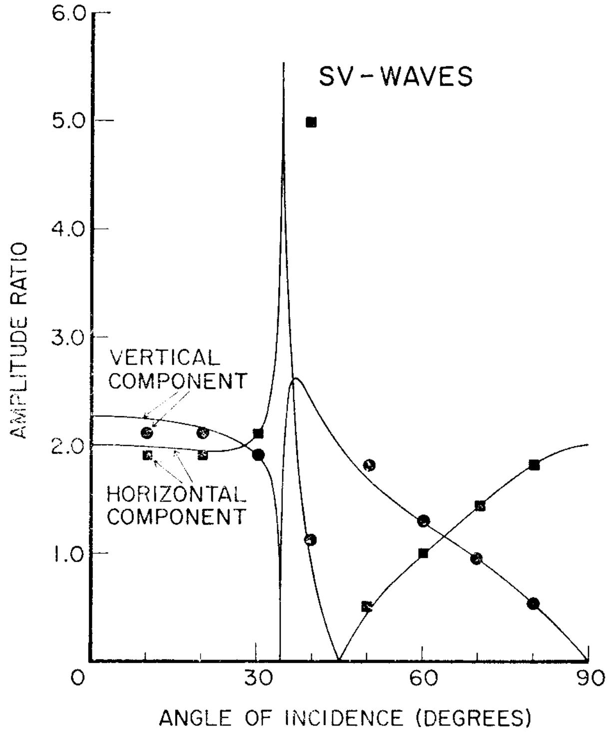

FIG. 5. Same as Fig. 4 for *SV*-waves (Appendix equations (A3)–(A6)). The computed waveforms for 30° to 80° are shown in Fig. 6.

ponents of motions derived from the model calculations. For *P*-waves, as discussed by Kawasaki *et al.* (1973), the free surface does not greatly affect the wave shape, and the calculations agree well with the theory.

Because the *SV* displacements are strongly modified by the free surface, they are shown for both the half space and the whole space in Fig. 6 for stations at 30–80 degrees. The station at 30 degrees is not beyond the critical angle (34·7°), there is no phase shift, and the wave shapes are similar. For the other stations, we must actually apply the theoretical phase shift to determine how well the calculations agree with theory. To evaluate the effect of this phase shift, consider an incident waveform $f(t)$ with Fourier transform $F(\omega)$. The Fourier transform of the surface motion is, using formula (A5) or (A6), $U(\omega) = R\,e^{i\delta sgn(\omega)}\,F(\omega)$, where R is $|RXS|$ or $|RZS|$, and $\delta sgn(\omega)$ is the corresponding phase shift. Applying the inverse transform to obtain the surface motion gives:

$$u(t) = \frac{1}{2\pi}\int_{-\infty}^{\infty} Re^{i\delta sgn(\omega)}\,F(\omega)e^{i\omega t}\,d\omega = R\cos\delta\, f(t) + R\sin\delta\, H(f(t))$$

where

$$H(f(t)) \equiv \frac{1}{\pi}\int_{0}^{\infty} d\omega \int_{-\infty}^{\infty} f(\tau)\sin\omega\,(\tau - t)\,d\tau.$$

The function $H(f(t))$ is the Hilbert transform of $f(t)$, discussed in more detail by Choy & Richards (1975).

The phase shifted, amplitude corrected, whole space *SV*-waves are compared with

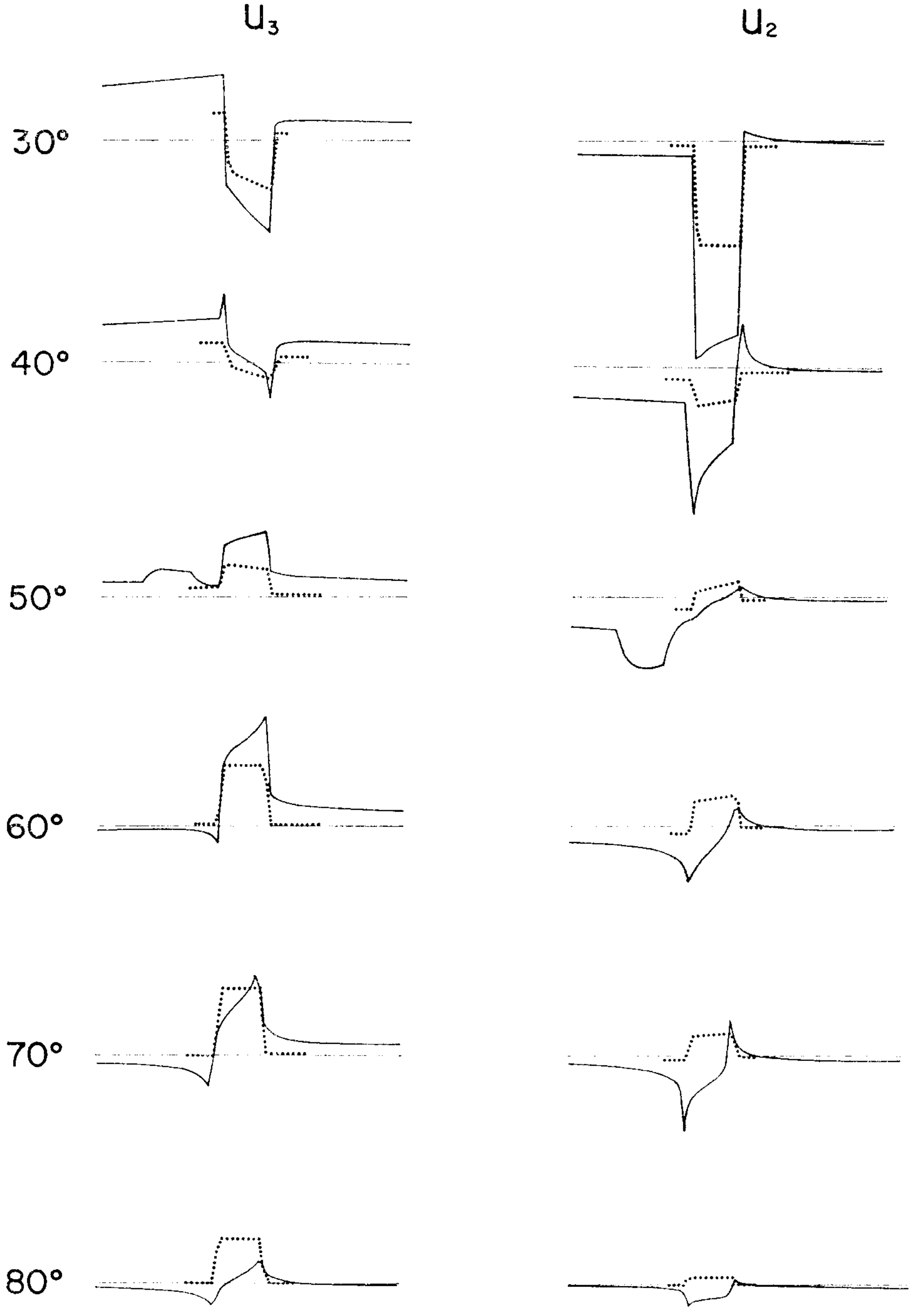

FIG. 6. Vertical (u_3) and horizontal (u_2) components of *SV*-waveforms for a half-space (solid) and an infinite-space (dotted) from a point source. For the source, $d = 10{\cdot}0$ km, $(S_1, S_3) = (0, S)$, and $\delta = 90°$. The stations are at $(x_1, x_2) = (0$ km, 10 tan (angle of incidence) km). The source has a rise time $= 0{\cdot}1$ s.

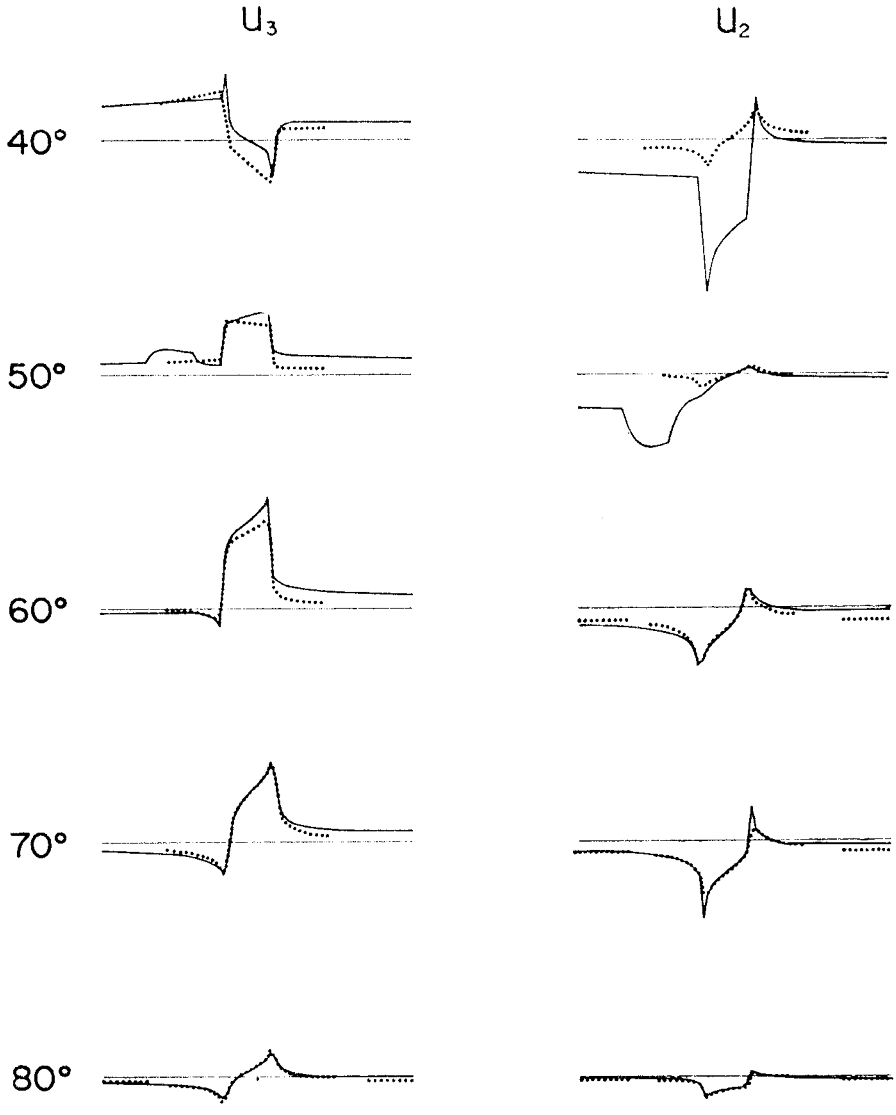

FIG. 7. Similar to Fig. 6, but the free surface amplitude and phase corrections for plane *SV*-waves (equations (A5) and (A6)) have been applied to the infinite space waveforms. In some cases, the infinite space waveform has also been arbitrarily shifted up or down. This is justified because near-field components are not amplified the same as the far-field *SV*-waves compared here. Where shifted, the dotted lines which are disconnected from the *S*-wave (as at 80°) show the zero for the whole space waveform.

the half-space waves in Fig. 7. Except at 40° and 50° the exact wave shapes and amplitudes agree well with those found by applying the plane wave correction. At 40° the displacements show practically no resemblance to each other. At 50° there are lesser differences, and another phase arrives before the *SV*-wave. This is the *SP*-phase. At 40°, this phase is superimposed on the *S*-wave, and is perhaps the sole cause of the disagreement. Although for angles greater than 50° the *SP*-phase has moved out of the time window in Fig. 7, it appears out to 80°, with a shape similar to the *SP*-phase at 50°, but decreasing amplitudes relative to the *S*-wave. As at 40° and 50°, amplitudes of the *SP*-phase may be larger than the *S*-wave, but in Fig. 7 it appears to be depleted in high frequencies relative to the *S*-wave.

The second objective of comparing displacements from a point dislocation in a half and an infinite space was to study the amplification of near and intermediate field components. These displacements cannot be separated for individual study as were the far-field terms. But at times when far-field terms are absent, the ratios of the half space to the infinite space displacements reveal the net effect of the free surface upon any near field or intermediate field terms which are present. This net effect is complex, and in general is not well described by the approximation that the free surface causes the amplitudes to double.

Because the stations are on the x_2 axis (Fig. 1, Fig. 6 caption), the *SH* case causes only U_1 displacements and the $P-SV$ case causes only U_2 (horizontal) and U_3 (vertical) displacements. In speaking of the near and intermediate field terms, it is better to refer only to the U_1, U_2 and U_3 components to remove the connotation of phases travelling only with the *P*- and *S*-velocities.

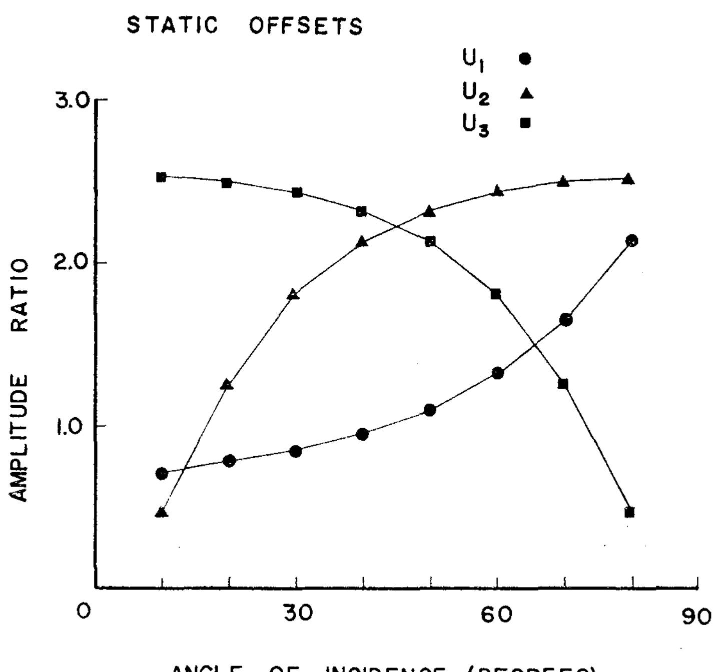

FIG. 8. Ratio of static offsets in a half-space to those in a whole-space for a point source with depth $d = 10$ km, and at stations $(x_1, x_2) = (0$ km, $10 \tan$ (angle of incidence) km). The u_1 component is derived for the source $(S_1, S_3) = (S, 0)$; the u_2 and u_3 components are derived for the source $(S_1, S_3) = (0, S)$. The lines only connect points derived from the models.

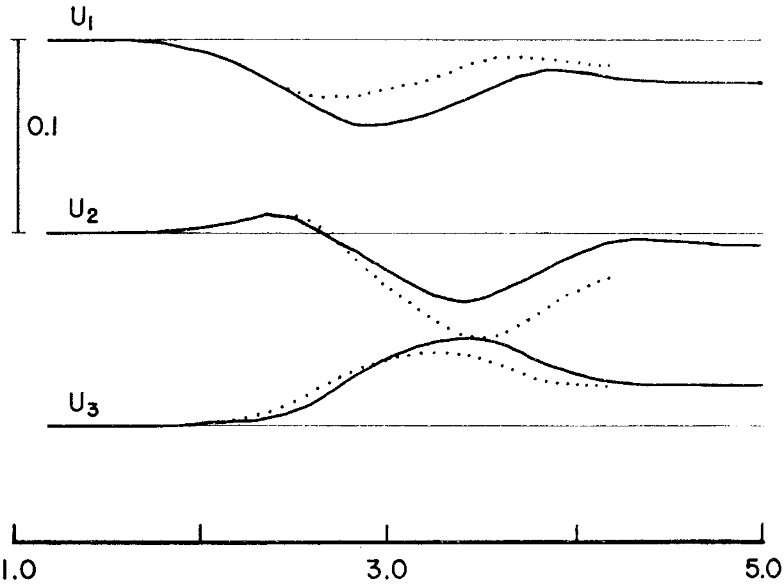

FIG. 9. Comparison of half-space (solid line) and doubled whole-space (dotted line) displacements for the dip-slip fault with $d = 3{\cdot}8$ km, $(x_1, x_2) = (5{\cdot}0$ km, $1{\cdot}5$ km), $\delta = 90{\cdot}0°$, $(S_1, S_3) = (0, S)$. Rupture parameters are $L_1 = 5{\cdot}0$ km, $L_3 = 3{\cdot}3$ km, $v = 3{\cdot}0$ km s^{-1}, and $\tau = 1{\cdot}0$ s. The vertical scale is in units of D_0 and the time scale is in seconds.

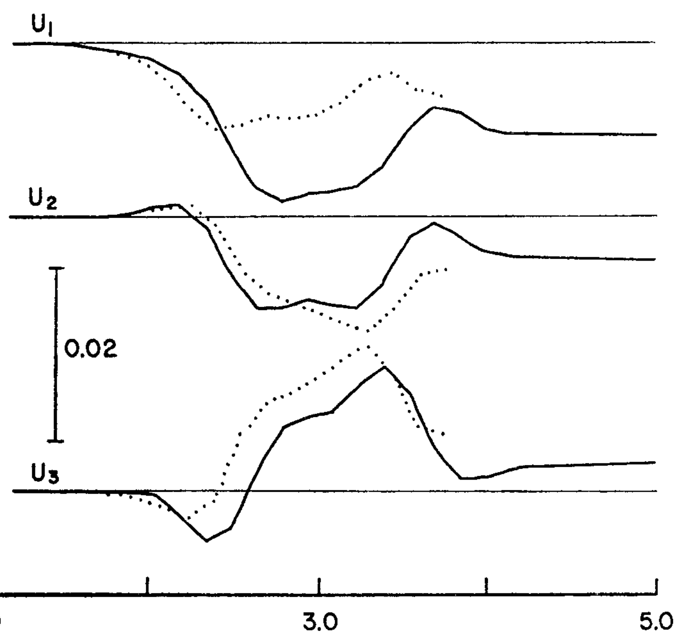

FIG. 10. Comparison of half-space (solid line) and doubled whole-space (dotted line) displacements for the dip-slip fault with $d = 1{\cdot}1$ km, $(x_1, x_2) = (5{\cdot}0$ km, $1{\cdot}5$ km), $\delta = 90{\cdot}0°$, $(S_1, S_3) = (0, S)$. Rupture parameters are $L_1 = 5{\cdot}0$ km, $L_3 = 1{\cdot}2$ km, $v = 3{\cdot}0$ km s^{-1}, $\tau = 1{\cdot}0$ s. The vertical scale is in units of D_0 and the time scale is in seconds.

Immediately after the P-wave, the amplitude ratio for each component resembles the amplitude ratio for the horizontal component of the P-wave (Fig. 4). Just before the S-wave, the ratio for each component, where it could be measured, had increased to a value generally in the range of 2·5–2·8. This ratio could not be measured for the U_2 and U_3 components incident at angles greater than 30 degrees because in these cases the SP-wave and the phase shift of the S-wave also cause displacements in the half-space before the theoretical S-wave arrival time.

The static offset ratios for all these components, shown in Fig. 8, generally differ from 2·0. These ratios, like the ratios of far-field components, are independent of the distance between the source and the station. For angles of incidence less than 30 degrees these ratios differ considerably from the amplification ratios of far-field body waves. Thus, it appears that even when the dynamic displacements of the surface of a half-space can be approximated by twice the infinite-space displacements, the static displacements cannot be reliably approximated in this way.

In summary, the amplification and phase shift of the far-field components of displacement close to a point dislocation can be understood well by applying plane wave theory. The theoretical amplification of plane waves does not apply to the static offset or to the amplification of near-field components of dynamic displacements, and it cannot, of course, explain the SP-phase or the Rayleigh wave.

Numerical examples: extended dislocation sources

For a small earthquake (resembling a point source), Figs 4–7 show that doubling infinite space motions is inadequate for stations with an angle of incidence of over 30 degrees if there is any SV motion, and nearly always inadequate if the angle of incidence is greater than 70 degrees. For an extended source, however, the contribution from each Green's function is only a small part of the total motion at the station.

Therefore Figs 9–13 were drawn to study half-space and whole-space motions for extended vertical faults. The fault motion is dip slip for the models in Figs 9 and 10, so that SV motion dominates, and strike slip for the models in Figs 11–13, so that SH motion dominates. The angles of incidence from the major fraction of fault planes are in three ranges: 30–60° (Figs 9 and 11), 60–80° (Figs 10 and 12), and over 80° (Fig. 13). In these cases, waveforms are low pass filtered with a corner at f_s to diminish higher frequency noise such as shown in Fig. 2.

Half-space motions are different from the doubled whole space motions for the dip-slip fault (Figs 9 and 10). In going to higher angles of incidence, the relative amount of SV motion increases and the whole space motions agree less with the half-space motions. The static offsets, determined by the last value each component attains, generally differ between the models. A dislocation in an infinite space to model the motions in the half space would probably not have rupture parameters similar to those used to calculate the half-space motions.

For the strike-slip faults (Figs 11–13), the horizontal displacements (including the static offset) derived from the whole space model resemble fairly well the half-space motions, with the exception of the clear Rayleigh wave on the u_1 component in Fig. 13. At 60–80 degrees, which contains less P–SV motions than 30–60 degrees, the doubled whole space motions approximate the half-space motions better than at 30–60 degrees. Above 80 degrees, the Rayleigh wave causes the agreement to worsen. The vertical (u_3) components are similar in Fig. 11, but in Figs 12 and 13 they are not. The horizontal static offsets from the whole space models match the static offsets of the half-space models. This is not expected considering the offsets for point sources shown in Fig. 8. A dislocation model in an infinite space would have similar rupture parameters to those used to calculate the half-space motions, providing the vertical component was ignored where appropriate.

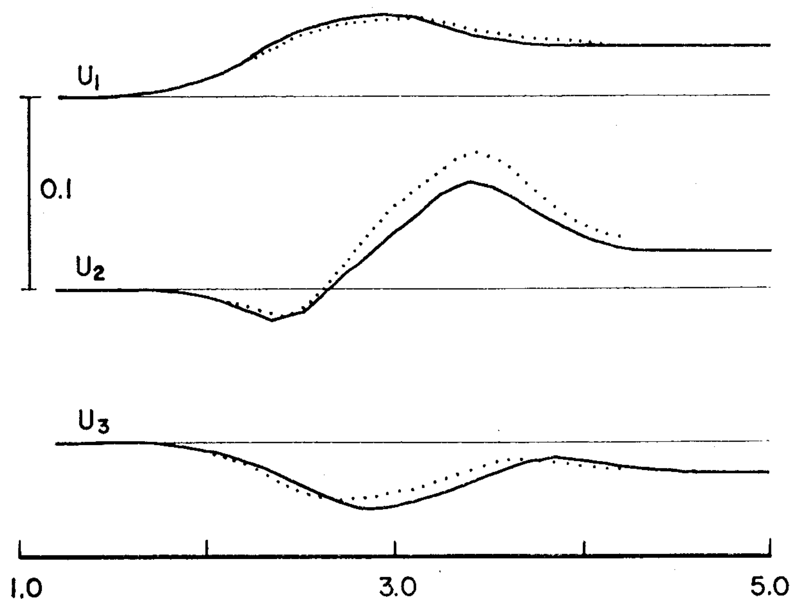

FIG. 11. Same as Fig. 9, but here for a strike slip fault with $(S_1, S_3) = (S, 0)$.

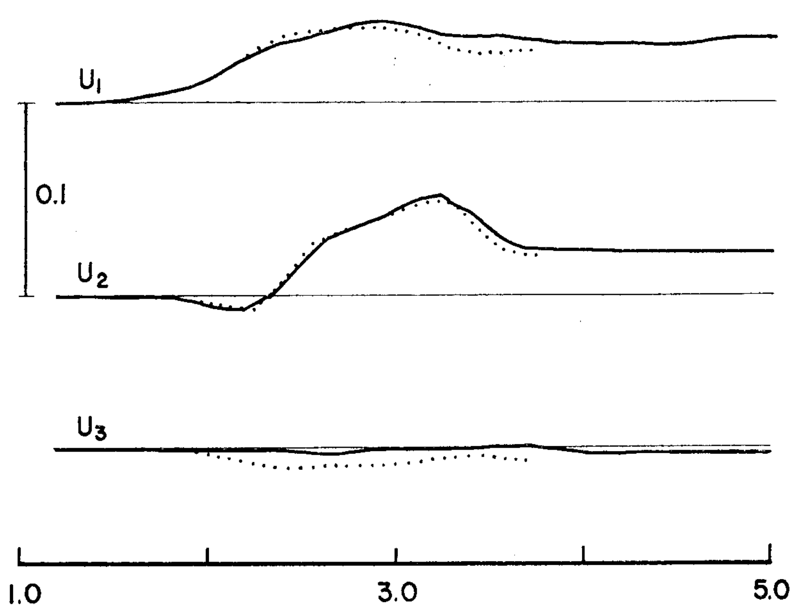

FIG. 12. Same as Fig. 10, but here for a strike slip fault with $(S_1, S_3) = (S, 0)$.

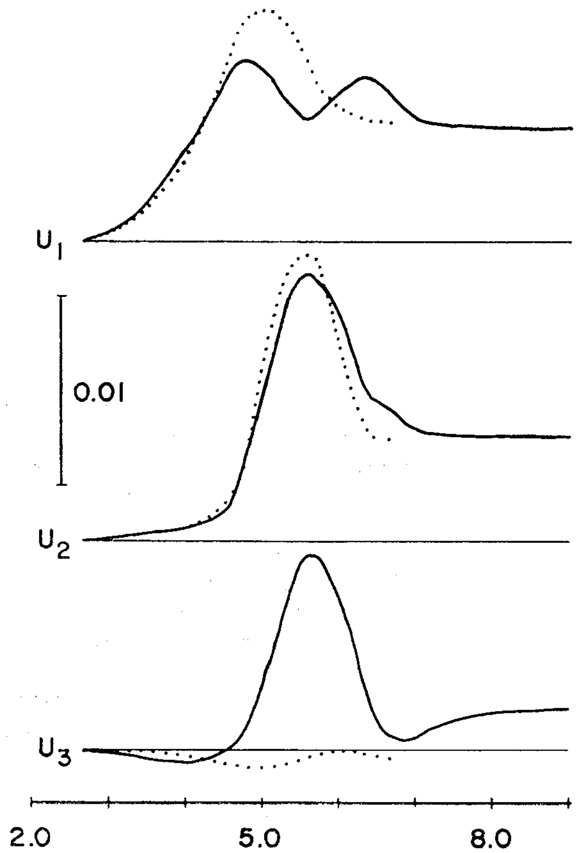

FIG. 13. Half-space (solid line) and doubled whole-space (dotted line) displacements for the strike slip fault with $d = 0{\cdot}5$ km, $(x_1, x_2) = (10{\cdot}0\text{ km}, 5{\cdot}45\text{ km})$, $\delta = 90°$, $(S_1, S_3) = (S, 0)$. Propagating ramp model parameters are $L_1 = 10{\cdot}0$ km, $L_3 = 0{\cdot}5$ km, $v = 3{\cdot}0\text{ km s}^{-1}$, $\tau = 1{\cdot}0$ s. The vertical scale is units of D_0 and the time scale is in seconds.

The u_1 and u_3 components in Fig. 13 show a strong Rayleigh wave, clearly identified by comparison with the whole space model. Pekeris & Lifson (1957) showed that for distances r and source depths z, the Rayleigh wave is emerging for $r/z = 5$ and clearly seen for $r/z = 10$. These ratios correspond to angles of incidence of about 79 and 84 degrees respectively. Thus, Figs 9–12 do not show a Rayleigh wave.

The Parkfield and San Fernando earthquakes have been studied extensively using high quality, close distance accelerograms to derive source dislocation models. Table 1 presents the fraction of the faults for these two cases which give direct ray angles to the accelerograph in the ranges 0–30, 30–60, 60–80 and 80–90 degrees. These percentages are estimated for a fault in a homogeneous half-space using the geometry of Trifunac (1974) for the San Fernando earthquake and of Anderson (1974) for the Parkfield earthquake. Even at the closest stations to the fault, at most about 20 per cent of the fault is in the 0–30 degree range. The remaining 80 per cent of the fault, including the epicentres, is in the range where the free surface may significantly distort the waveform derived from the whole space approximation. The San Fernando earthquake had a thrusting mechanism while the Parkfield earthquake had a strike-slip mechanism, and thus S-waves from the San Fernando earthquake at nearby stations would in general have a greater component of SV-type motion. Therefore, when the infinite space method is used, rupture parameters derived for the San Fernando earthquake are more likely to be incorrect than rupture parameters derived for the Parkfield earthquake.

Table 1 indicates that even at the best-placed instruments, angles of incidence are likely to be high for most of the fault plane. This is especially indicated by the angles of incidence of the Pacoima Dam accelerograph. In this case, the instrument was located directly above the fault, and yet SV-types wave from only about 20 per cent of the fault plane would be relatively undistorted by the free surface.

Conclusions

A practical way of computing displacements on the surface of a half-space is by a two step process. The first step is calculating and storing the Green's function for a given station for a grid of points on the fault; and the second step is convolving with the source-time function. In studying a particular accelerogram record, this method is far more economical than it would be to recompute the Green's functions for each trial source function. This two step method also gives a clear idea of what frequencies are significant in the calculated displacement record.

The dynamic displacement of the surface of a half-space caused by an extended dislocation source generally differs from two times the displacement which would result from the same source in an infinite space. There are two exceptions.

The first exception is a fault located such that angles of incidence at the station are less than 30 degrees from vertical. For a large fault, however, even at the best-placed instruments, the angles of incidence will be this small from only a small fraction of the fault. This case is therefore most useful for studying small earthquakes. The static offset estimated from the infinite space method may be wrong in this case, but this is not of practical importance as most data cannot resolve such offsets.

The second exception occurs when the motion at the source is predominantly strike slip. Then the horizontal components may be modelled by the infinite space motion when the Rayleigh wave is not important (e.g. for angles of incidence less than 80°). The vertical component in this case may also be used for angles of incidence less than about 60 degrees. This case will be most useful for studying strike-slip earthquakes.

Table 1

Estimated fraction (nearest 5 per cent) of fault area within each range of angle of incidence

	Angle of Incidence (degrees)			
Earthquake/Station	0°–30°	30°–60°	60°–80°	80°–90°
Parkfield				
Cholame–Shandon #2	10	20	50*	20
Cholame–Shandon #5	0	25	55*	20
Cholame–Shandon #8	0	15	65*	20
Cholame–Shandon #12	0	5	65*	30
Temblor	0	10	60*	30
San Fernando				
Pacoima Dam	20	45*	25	10
Castaic Old Ridge Route	0	0	15*	85
Palmdale Fire Station	0	0	20*	80
Jet Propulsion Laboratory	0	0	45*	55
8244 Orion Blvd	0	0	75*	25

* The epicentre is in this range.

In many cases, a small earthquake recorded at a large angle of incidence can be modelled using the infinite space method. When the observed S-wave is separated from other phases, and near-field terms are small, it can be separated into SV- and SH-components. Then the phase shift and amplitude correction can be applied to each component separately to obtain the incident waveforms, for comparison with infinite space models.

Acknowledgments

P. G. Richards, L. E. Alsop and J. Nafe critically reviewed the manuscript. K. Nagoa and G. Anderson helped with the drafting. Computer time was supplied by the Goddard Institute of Space Studies in New York City. This research was supported by the Advanced Research Projects Agency of the Department of Defense, and was monitored by the Air Force Office of Scientific Research under Contract No. F44620-74-C-0029.

Lamont-Doherty Geological Observatory Contribution No. 2353.

References

Anderson, J., 1974. A dislocation model for the Parkfield earthquake, *Bull. seism. Soc. Am.*, **64**, 671–686.

Anderson, J. G. & Richards, P. G., 1975. Comparison of strong ground motion from several dislocation models, *Geophys. J. R. astr. Soc.*, **42**, 347–373.

Ben-Menahem, A., 1961. Radiation of seismic surface waves from finite moving sources, *Bull. seism. Soc. Am.*, **51**, 401–435.

Burridge, R. & Knopoff, L., 1964. Body force equivalents for seismic dislocations, *Bull. seism. Soc. Am.*, **54**, 1875–1885.

Choy, G. L. & Richards, P. G., 1975. Pulse distortion and Hilbert transformation in multiply reflected and refracted body waves, *Bull. seism. Soc. Am.*, **65**, 55–70.

Hales, A. L. & Roberts, J. L., 1974. The Zoepritz amplitude equations: more errors, *Bull. seism. Soc. Am.*, **64**, 285.

Haskell, N. A., 1969. Elastic displacements in the near-field of a propagating fault, *Bull. seism. Soc. Am.*, **59**, 865–908.

Johnson, L. R., 1974. Green's function for Lamb's problem. *Geophys. J. R. astr. Soc.*, **37**, 99–131.

Kanamori, H., 1972. Determination of effective tectonic stress associated with earthquake faulting. The Tottori earthquake of 1943, *Phys. Earth planet. Int.*, **5**, 426–434.

Kawasaki, I., Suzuki, Y. & Sato, R., 1973. Seismic waves due to a shear fault in a semi-infinite medium. Part I: Point sources, *J. Phys. Earth*, **21**, 251–284.

Knopoff, L., Fredericks, R. W., Gangi, A. F. & Porter, L. D., 1957. Surface amplitudes of reflected body waves, *Geophysics*, **22**, 842–847.

Pekeris, C. L. & Lifson, H., 1957. Motion of the surface of a uniform elastic half space produced by a burried pulse, *J. acoust. Soc. Am.*, **29**, 1233–1238.

Sato, R. & Matsuura, M., 1974. Strains and tilts on the surface of a semi-infinite medium, *J. Phys. Earth*, **22**, 213–221.

Trifunac, M. D., 1974. A three-dimensional dislocation model for the San Fernando, California, earthquake of February 9, 1971, *Bull. seism. Soc. Am.*, **64**, 149–172.

Trifunac, M. D. & Udwadia, F. E., 1974. Parkfield, California, earthquake of June 27, 1966: A three dimensional moving dislocation model, *Bull. seism. Soc. Am.*, **64**, 511–533.

Wilf, H. S., 1967. Advances in numerical quadrature, *Mathematical Methods for Digital Computers*, *Vol. II*, 133–137, eds A. Ralston & H. S. Wilf, John Wiley and Sons, Inc., New York.

Appendix 1

Derivation of amplification coefficients for body waves incident on a free surface

The ratio of the amplitude of each component of the free surface motion to the amplitude of the same component of an incident body wave is derived here. Knopoff *et al.* (1957), who derive the ratio of each component to the total amplitude of the incident wave, have some misprints which make this derivation necessary. In equation (6), a quantity they refer to as tanh θ' is always greater than 1; in equation (7), the phase is incorrect in the centre of the three equalities because tan 2ϕ changes sign at 45°; and in equation (9) (substituting 'tanh θ'' as defined), the phase does not agree with Fig. 3. The figures in Knopoff *et al.* are correct. The closely-related equations for reflection and transmission coefficients at a boundary between two layers have a long history of published errors (Hales & Roberts 1974).

We first discuss the problem of a plane P-wave incident with angle i and a plane SV-wave incident at angle j; both incident from $z < 0$ on a free surface $z = 0$; and both waves having horizontal slowness s. Later, we will specialize to the case where only one of these waves is incident.

The total wave field is described by displacement

$$\mathbf{u} = \operatorname{grad}\phi + \operatorname{curl}(\mathrm{o}, \Psi, 0) = \left(\frac{\partial\phi}{\partial x} - \frac{\partial\Psi}{\partial z}, 0, \frac{\partial\phi}{\partial z} + \frac{\partial\Psi}{\partial x}\right)$$

where

$$\begin{aligned}\phi &= P_i f\left(t - sx - z\frac{\cos i}{\alpha}\right) + P_r f\left(t - sx + z\frac{\cos i}{\alpha}\right)\\ &= \phi_i \qquad\qquad\qquad\qquad\quad + \phi_r\\ \Psi &= S_i f\left(t - sx - z\frac{\cos j}{\beta}\right) + S_r f\left(t - sx + z\frac{\cos j}{\beta}\right).\end{aligned}$$

Here the first term on the right represents the incoming wave in each case, and the second term represents the outgoing reflected wave. In these equations $f(t)$ denotes the time dependence of the potentials,

$$s = \frac{\sin i}{\alpha} = \frac{\sin j}{\beta}$$

is the horizontal slowness, α is the P-wave velocity, and β is the S-wave velocity. The terms P_i and S_i are constants, and P_r and S_r are unknowns to be derived from the free surface boundary conditions of zero traction on $z = 0$.

These boundary conditions yield the equations:

$$(P_i - P_r)\frac{\sin 2i}{\alpha^2} - (S_i + S_r)\frac{\cos 2j}{\beta^2} = 0$$

$$(P_i + P_r)\cos 2j + (S_i - S_r)\sin 2j = 0,$$

which have the solution

$$P_r = P_i\left(\frac{1}{D}\right)\left(\frac{\sin 2i \sin 2j}{\alpha^2} - \frac{\cos^2 2j}{\beta^2}\right) + S_i\frac{1}{D}\left(-2\frac{\sin 2j\cos 2j}{\beta^2}\right)$$

$$S_r = P_i\left(\frac{1}{D}\right)\left(2\frac{\sin 2i\cos 2j}{\alpha^2}\right) + S_i\frac{1}{D}\left(\frac{\sin 2i \sin 2j}{\alpha^2} - \frac{\cos^2 2j}{\beta^2}\right)$$

where

$$D = 2s\frac{\cos i}{\alpha}\sin 2j + \frac{1}{\beta^2}\cos^2 2j.$$

The desired ratios are the amplitude of a component of the motion of the free surface ($z = 0$) due to either an incident P-wave ($S_i = 0$) or SV-wave ($P_i = 0$) divided by the *same component* of motion which would take place if the surface were absent. For example,

$$RXP = \frac{u_x^P(\frac{1}{2})}{u_x^P(\infty)} = \frac{\left\{-P_i s - P_r s - S_r \frac{\cos j}{\beta}\right\}}{-P_i s}.$$

Here u_x^P refers to the horizontal (x) component of P-wave motion, and the ($\frac{1}{2}$) or (∞) refer to the case of a half space and of an infinite space respectively.

For incident P-waves, the ratios are:

$$RXP = \frac{2\sin 2i \cot j}{\alpha^2 D} \tag{A1}$$

$$RZP = \frac{2\cos 2j}{\beta^2 D}. \tag{A2}$$

For S-waves incident at angles less than the critical angle j_c ($\sin j_c = \beta/\alpha$), the ratios are:

$$RXS = \frac{2\cos 2j}{\beta^2 D} \tag{A3}$$

$$RZS = \frac{4s\cos i \cot j}{\alpha D}. \tag{A4}$$

For S-waves incident at angles greater than critical, a phase shift is introduced. At this point, it is necessary to consider a specific frequency component: $f(t) = e^{i\omega t}$. Then for $j > j_c$ the quantity $\cos i/\alpha$ is replaced by an imaginary quantity $-ib\,\mathrm{sgn}(\omega)$, where the sign is chosen so that the potential ϕ_r will decrease with increasing distance from the free surface. Here $\mathrm{sgn}(\omega) = 1$ if $\omega > 0$ and -1 if $\omega < 0$, and $b = \sqrt{(s^2 - \alpha^{-2})}$. Then the ratios for $j > j_c$ are:

$$RXS = \left|\frac{2\cos 2j}{\beta^2 D'}\right| \exp(i(p+\theta)) \tag{A5}$$

$$RZS = \left|\frac{4sb\cot j}{D'}\right| \exp\left(i\left(p - \frac{\pi}{2}\,\mathrm{sgn}(\omega)\right)\right) \tag{A6}$$

where

$$D' = \left[\left(\frac{\cos 2j}{\beta}\right)^4 + (2sb\sin 2j)^2\right]^{\frac{1}{2}}$$

$$\tan p = \frac{2\beta^2 sb\sin 2j}{\cos^2 2j}\,\mathrm{sgn}(\omega)$$

$$\text{and } \theta = \begin{cases} 0 & j_c < j \leqslant \pi/4 \\ \pi & \pi/4 < j < \pi/2 \end{cases}$$